Statistical Studies of Plasma Structuring in the Auroral Ionosphere by the Swarm Satellites

L. M. Buschmann[1] , **L. B. N. Clausen[1]** , **A. Spicher[2]** , **M. F. Ivarsen[1,3]** , and **W. J. Miloch[1]**

[1]Department of Physics, University of Oslo, Oslo, Norway, [2]Institute for Physics and Technology, UiT—The Arctic University of Norway, Tromsø, Norway, [3]Department of Physics and Engineering Physics, University of Saskatchewan, Saskatoon, SK, Canada

Abstract This study uses over 2 years of 16 Hz density measurements, 50 Hz magnetic field data and ROTI data from the Swarm mission to perform long term statistics of plasma structuring in the polar ionosphere. The timeframe covers more than 2 years near the 24th solar cycle peak. We additionally use 3 years of data obtained from a timeframe close to solar minimum for discussion. We present power spectral densities (PSD) of electron density irregularities and magnetic field for 1-min intervals. These PSD have been characterized by the probability of a slope steepening, and by integrating the power deposited within frequency intervals corresponding to kilometer scales. For the electron density, we observe seasonal dependencies for both the integrated power and slope characteristics. While the dual slope probability, especially within the polar cap, varies with solar EUV-radiation, the integrated power is strongest around the equinoxes. Additionally, while we found similar results for the slope probability for both hemispheres, the integrated power exhibits strong hemispheric asymmetries with stronger enhancements within local summer in the southern hemisphere. The ROTI data shows a similar seasonal variability as the density PSD integrated power, in both seasonal dependency and interhemispheric variability. However, for the ROTI data the strongest fluctuations were found within the nightside auroral oval and the cusp. For the PSD of the magnetic field data, we obtain the strongest enhancements within the cusp for all seasons and all hemispheres. The fluctuations may indicate an increase in Alfvénic energy associated with a downward Poynting flux.

1. Introduction

Auroral particle precipitation is believed to be a major source of large scale irregularities in the plasma of the cusp and night-side auroral oval (M. C. Kelley et al., 1982; Moen et al., 2013, 2002). Precipitating electrons can protrude into the ionosphere in these regions and function as a source of free energy. Large-scale irregularities that evolve in the cusp can follow the polar convection pattern toward the night side through the polar cap (PC) and constitute a crucial factor for the development of structures in the polar cap. The most noteworthy among these structures are polar cap patches (PCP).

PCP can be defined as areas with scales between 100 and 1,000 km which have at least twice the density of the background plasma. These patches are generated when high density solar-EUV produced plasma on the dayside ionosphere enters the polar cap (Carlson, 2012; Crowley et al., 1996 and references therein). When these structures travel through the PC, they can be broken down to smaller scales, in a so-called turbulent cascade. Several sources have been proposed to explain the formation of these irregularities, including the gradient drift instability (GDI) and the Kelvin-Helmholtz instability (KHI) (S. Basu et al., 1990; Carlson, 2012; M. J. Keskinen & Ossakow, 1983; Kintner & Seyler, 1985; Tsunoda, 1988). The GDI affects primarily the trailing edge of PCP as the background plasma flow is parallel to the gradient of the electron density (Tsunoda, 1988). On the other hand, the KHI is driven by velocity shears in the plasma. Lately, a two-step process has been proposed in which patches are first structured by shear driven instabilities (e.g., the KHI) in the first minutes after the patch enters the PC. In a second step the GDI is then taking over and is further structuring the patch into decameter scale irregularities (Carlson, 2012; Carlson et al., 2007; Hosokawa et al., 2013; Moen et al., 2012, 2013).

Several studies have been conducted with focus on PCP, showing a seasonal dependency of the occurrence of irregularities. Generally, a higher occurrence of patches has been found in the northern hemisphere (NH) during winter season (Chartier et al., 2018; Jin & Xiong, 2020). Overall, polar cap patches are more subdued in summer due to the background plasma from elevated EUV ionization (Spicher et al., 2017). As the majority of these

studies have been conducted in the NH, less studies involve the southern hemisphere with contradictory results (Chartier et al., 2018, 2019; David et al., 2019; Jin & Xiong, 2020; Kagawa et al., 2021; Spicher et al., 2017).

When these larger scale structures are broken down to smaller scales, they can cause problems for global navigation satellite systems (GNSS). Scintillations, which are rapid temporal fluctuations in phase and amplitude in trans-ionospheric GNSS signals, can be detrimental for navigation accuracy or signal acquisition (S. Basu et al., 1990; Kintner et al., 2007; Tsunoda, 1988; Yeh & Liu, 1982). Below the Fresnel's scale, which is of the order of few hundreds of meters for GNSS signals, the scintillations of phase and amplitude are of stochastic nature and due to diffractive effects (Kintner et al., 2007). Above the Fresnel scale, refraction effects, which are of deterministic nature, become important and can result in enhanced values of phase scintillation index σ_Φ (McCaffrey & Jayachandran, 2019). They can often be removed by applying ionospheric free-linear combination (IFLC), where a combination of two carrier phases of two signals with different frequencies are used to remove refractive effects on the signals (Carrano et al., 2013; Zheng et al., 2022). Enhancements in σ_Φ indices have also been shown to be adequately represented by ROTI on larger scales above the Fresnel scale (Rino et al., 2019), and can additionally be dependent on the plasma flow and rate of change of TEC (ROT) at high latitudes (Y. Wang et al., 2018, 2022). Recent literature has proposed that only fluctuations of the former nature, namely of stochastic nature, are deemed scintillations (De Franceschi et al., 2019; Ghobadi et al., 2020; McCaffrey & Jayachandran, 2019; Spogli et al., 2021).

It has been shown that high levels of σ_Φ can be related to particle precipitation in the cusp aurora (Clausen et al., 2016; Jin et al., 2015, 2017) and that filamentary field-aligned currents (FAC), are co-located with strong enhancements in σ_Φ in the cusp (Fæhn Follestad et al., 2020). As GNSS have become increasingly important, research on plasma irregularities in the ionosphere and associated effects has intensified in recent years (Jin et al., 2014, 2017; Kintner et al., 2007; Moen et al., 2012, 2013; Oksavik et al., 2012; van der Meeren et al., 2015).

One method to investigate instabilities and turbulence in plasmas comprises the use of spectral analysis (Frisch & Kolmogorov, 1995). Ionospheric plasma instabilities have been suggested to follow power laws with different mechanisms resulting in different slopes when fitted in a plot with double logarithmic axes (Kintner & Seyler, 1985; Tsunoda, 1988). Previous observations suggest an initial slope, or spectral index, between 1 and 2.2, depending on the altitude and region (B. Basu & Coppi, 1988; S. Basu et al., 1990; M. Kelley et al., 1982; M. C. Kelley et al., 1982; Kintner & Seyler, 1985; LaBelle et al., 1986; Pfaff et al., 1997; Prakash et al., 1971). In situ measurements of the ionosphere reveal that plasma fluctuations exhibit a steeper slope at higher frequencies. This slope steepening was first documented for the low-latitude ionosphere using sounding rockets and satellites (M. C. Kelley et al., 1982) and is commonly observed in this region (Hysel et al., 1994; Jahn & LaBelle, 1998; LaBelle et al., 1986). The high-latitude F-region has also shown this steepening (S. Basu et al., 1990; Buschmann et al., 2023; Di Mare et al., 2021; Ivarsen et al., 2019, 2021; Spicher et al., 2014; Villain et al., 1986). The spectral index in the high-latitude ionosphere has been shown to be approximately $-5/3$ at low frequencies and around -3 to -5 at high frequencies. Spectral breakpoints, or the frequency at which the spectral steepening occurs, have been observed on a variety of scales ranging up to 100 Hz (Buschmann et al., 2023; Di Mare et al., 2021; Ivarsen et al., 2019, 2021; Spicher et al., 2014). Spectral break points at different scale sizes may indicate different mechanisms happening at different scales. Spectral breaks that have been observed by sounding rockets have often been linked to the oxygen gyrofrequency at the corresponding altitudes, a transition between the inertial regime to a collisional regime (M. Keskinen & Huba, 1990), the ion-inertial range (Di Mare et al., 2021; Ivarsen et al., 2019), or where diffusion, drift waves, or wave steepening dominate (Hysell et al., 1994; LaBelle et al., 1986). Another approach, in contrast to the dissipation of energy, links the spectral break to an injection of energy within these scales (Kintner & Seyler, 1985). The frequency at which the spectral break occurs has been studied for decades, but is still not fully understood (Tsunoda, 1988).

Recently, Ivarsen et al. (2021) used an automated spectral breakpoint algorithm to characterize power spectra from several years of electron density data showing a spectral index of -1.6 on average at larger scales throughout the F-region ionosphere. Additionally, they linked the occurrence of spectral steepening in the polar ionosphere to the level of solar extreme ultraviolet (EUV) radiation and thus the solar zenith angle (SZA), presenting evidence for the dependency of plasma irregularities in the polar cap on the SZA.

Lately it has been found that the occurrence of double slopes in the electron density was most prominent in the cusp and immediately poleward of the cusp, while the strongest electron density fluctuations were found just poleward of the cusp (Buschmann et al., 2023; Spicher et al., 2022). Additionally, an analysis of the integrated

spectral power in the power spectral density (PSD) showed an increased energy within lower frequencies in presence of particle precipitation, while power in higher frequencies is elevated poleward of the precipitation, suggesting an energy input from electron precipitation into the cusp in frequencies corresponding to kilometer scales, while the energy is cascading to smaller scales in the polar cap.

This study is conducted by using data from the Swarm satellites. An advantage of the Swarm mission, or polar orbiting satellites in general, is that there is coverage over all latitudes. This gives the opportunity to conduct statistical research for large time periods and different latitudes.

Section 3 of this study gives the results for high solar activity. We have analyzed data between 01 October 2014 and 31 December 2016, and between 01 January 2020 and 31 December 2022, to distinguish between differences in the processes for solar maximum and minimum, respectively. However, due to a larger amount of data gaps within the time frame 2020 to 2022 we decided to mainly focus on the years 2014–2016, a period that directly follows the 24th solar cycle peak. For completeness, the results for low solar activity will be given in Appendix A.

2. Methodology and Instrumentation

This study uses data from the Swarm mission, a satellite constellation consisting of three identical satellites (A, B, and C) (Friis-Christensen et al., 2006, 2008). We make use of data from satellites A and C, which are flying side-by-side (1.4° separation in longitude at the equator) at an altitude of around 460 km. The employed data includes the 16 Hz face-plate electron density (N_e), the 50 Hz magnetic field data (B), the field-aligned current (FAC) data, and the Rate of Change of TEC index (ROTI) from the Ionospheric Plasma Irregularities (IPIR) data set (Jin et al., 2022). The data set used covers a period of more than 5 years, from 01.10.2014 to 31.12.2016, and from 01.01.2020 to 31.12.2022, to distinguish between differences in the processes for solar maximum and minimum, respectively. For our analysis, we only use time intervals where all data sets are available, thus ensuring that N_e, B, FAC, and IPIR data are present for all intervals. We thus cover the majority of the chosen time frame, however, some larger data gaps can be found throughout the data. Moreover, in the statistical analysis we additionally only use data poleward of ±50° magnetic latitude. For conversion from geographic coordinates to magnetic latitude (MLat) and magnetic local time (MLT) we use magnetic apex coordinates (AD, 1995; Emmert et al., 2010). Additionally, we divide the data into 4 seasonal intervals, comprising 4 time spans between 91 and 92 days around the equinoxes and solstices. This leads to the following seasonal intervals: spring, utilizing data between 4 February and 5 May, summer between 6 May and 5 August, autumn between 6 August and 5 November, and winter between 6 November and 3 February.

For the 16 Hz N_e and 50 Hz B data, we conduct a spectral analysis using the Logarithmic frequency axis Power Spectral Density (LPSD) method as described in Tröbs and Heinzel (2006). This procedure utilizes the Welch power spectral method. The Welch power spectra is a method of estimating PSD by averaging modified periodograms (Welch, 1967). However, while the original Welch method is utilizing the same frequency resolution for every Fourier frequency, the LPSD method is adjusting the frequency resolution instead (Tröbs & Heinzel, 2006). As we are mainly interested in fluctuations of B and N_e rather than absolute values, we apply a first-order linear trend to both quantities for each 1-min interval prior to the spectral analysis, in order to get information about the small-scale fluctuations only and eliminate influence of seasonal dependencies in N_e. We then perform the spectral analysis mentioned above using a Hanning window for a 1-min interval. The resulting power spectrum can then be described by either one or two linear slopes in a plot with double logarithmic axes, with

$$\text{PSD}(f) \propto f^{-p} \tag{1}$$

where p is the slope of the fit and thus $p > 0$. For a power spectrum that is better described with two fits, the equation changes to

$$\text{PSD}(f) \propto \begin{cases} f^{-p_1}, & for\ f \leq f_{sb} \\ f^{-p_2}, & for\ f \geq f_{sb} \end{cases} \tag{2}$$

where f_{sb} is the break point frequency where the slopes p_1 and p_2 of the PSD change, with $p_2 > p_1$. We plot the power spectra for each interval using a logarithmic scale and then use an automated slope detection method, which fits one or two slopes to the spectrum using a piece-wise linear Hermite function as a least-square fit as described in
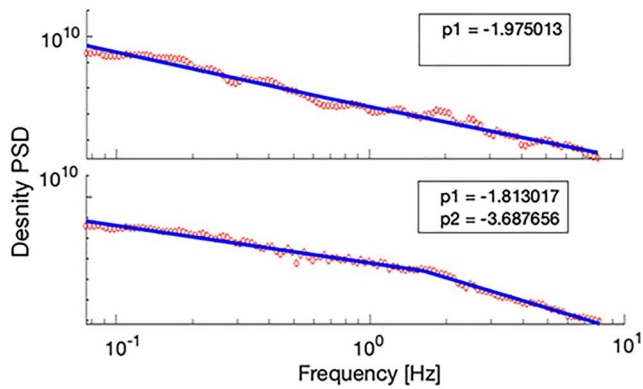
Figure 1. Power-spectral density plot of the electron density N_e. The top plot shows a PSD that is best approximated by a single linear trend (single slope, SS), while the bottom plot shows a PSD that is best approximated by a combination of two linear trends (double slope, DS).

D'Errico ([2017]). The method is minimizing the rms error in order to localize the spectral break frequency and is further described in Ivarsen et al. ([2019], [2021]). The threshold which is used to determine if two fitted slopes are considered a double slope is $p_2 - p_1 \geq 0.8$. This threshold has been used in previous works (Buschmann et al., [2023]; Ivarsen et al., [2019]) and has been determined by repeated testing. The range in which a break point could be found is set to frequencies between 0.19 and 7 Hz, which corresponds to spatial scales between 1.1 and 40 km, respectively. As N_e is measured at a cadence of 16 Hz, we are not able to obtain any information above 8 Hz within the PSD, which corresponds to the Nyquist frequency. Two examples of density PSD plots with either a single or double slope are shown in Figure [1].

In addition to the slopes and break-point, we analyze the integrated power within certain frequency intervals in order to compare the power within different spatial scales in different regions. For the analysis of N_e we choose a 1 Hz frequency interval between 1 and 2 Hz, which corresponds to spatial scales between 3.8 and 7.6 km. Additional intervals between 0.1 and 0.6 Hz and 6 and 7 Hz are analyzed for comparison. We also utilize the 10 s ROTI data obtained from the IPIR data set. ROTI is the standard deviation of Total Electron Content (TEC) for a given running window, in this case 10 s. The ROTI is calculated from the Vertical TEC (VTEC) values, the exact calculation and methodology for the ROTI derivation is documented in Jin et al. ([2022]).

We have added the ROTI data in addition to the integrated power analysis in order to get an additional source of data for comparison. The integrated power is calculated from the in situ measurements of the 16 Hz N_e PSD and thus provides a measure of the energy deposited within different frequency ranges. While this study mainly focuses on frequencies between 1 and 2 Hz, we also analyze the energy deposited within 0.1–0.6 Hz and 6–7 Hz for comparison. The integrated power thus provides a measure of the amplitude of fluctuations of certain scales. The ROTI data, on the other hand, covers a large ionospheric area as it is calculated from the GNSS receivers on board of the satellites and is thus not a direct measurement within the plasma, as it calculates the TEC based on the signals obtained from GNSS satellites. Thus, the ROTI data provides a measure of fluctuations within the plasma density and gives a measure of the amount of structuring.

The main FAC data used within this study stems from the B_y component of the 50 Hz B data, as described further in the next paragraph. In addition, for the first run of analyses we use the 1 Hz FAC product. This product uses simultaneous measurements of the constellation of both Swarm A and C. The calculation is based on the vertical current density using Ampere's law, the FAC is then obtained from the magnetic field residuals. A more in-depth calculation can be obtained from Ritter et al. ([2013]).

The 50 Hz B data analysis uses a similar technique as the analysis of N_e, only varying in the frequency interval used for detecting break points. As the sampling frequency for B is much higher than for the N_e sampling frequency, we set the interval to frequencies between 0.5 and 23 Hz, corresponding to spatial scales between 0.33 and 15.2 km. The interval chosen for the integrated power analysis is once more a 1 Hz interval, again between 1 and 2 Hz, corresponding to spatial scales between 3.8 and 7.6 km. We decided to use the B_y-component, or geographic east component in NEC-coordinates, as a proxy for the FAC, as it is not feasible to conduct a spectral analysis on the 1 Hz FAC data in this case, while the B data is provided at 50 Hz resolution. The magnetic field may be converted to the FAC density j_z according to Fæhn Follestad et al. ([2020]) and Ritter et al. ([2013])

$$j_z = \frac{1}{\mu_0 \nu_x} \frac{\Delta B_y}{\Delta t} \tag{3}$$

where ν_x is the velocity perpendicular to the FAC and ΔB_y is the detrended magnetic component parallel to the current sheet (Fæhn Follestad et al., [2020]; H. Wang et al., [2005]). We then use the fluctuations is B_y as a mean of analyzing the FAC.

Figure [2] shows a sample pass of Swarm A over the northern hemisphere on the 2nd November 2014 between 13:09 and 13:41 UT. The trajectory of the satellite can be seen in the upper right corner of Figure [2]. The figure shows N_e (panel a), FAC (panel b), B_y (panel c), slopes obtained from the N_e PSD and the corresponding spectral
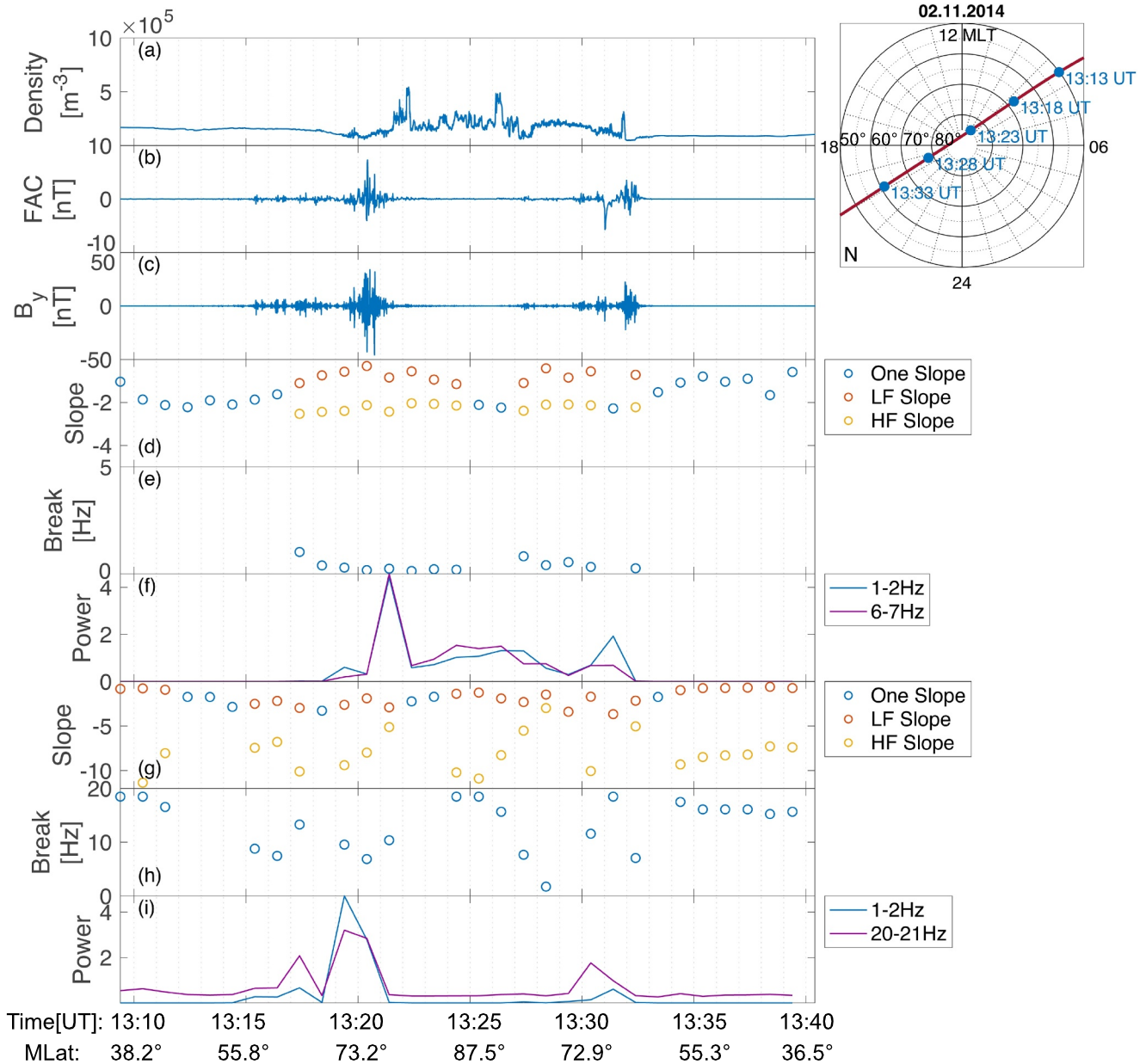
Figure 2. One pass of Swarm A over the polar region in the northern hemisphere on 02.11.2014 between 13:09 UT and 13:41 UT. The panels show the following from top to bottom, with frequencies giving the cadence of the corresponding signal: (a): the absolute 16 Hz electron density N_e, (b): the absolute 1 Hz FAC, (c): the detrended 50 Hz B_y-component, (d): the slopes obtained from the N_e PSD, and (e): the corresponding spectral break frequencies, (f): the integrated power from the N_e PSD between 1–2 and 6–7 Hz, (g): the slopes obtained from the B_y PSD, and (h): the corresponding spectral break frequencies, and (i): the integrated power from the B_y PSD between 4–5 and 20–21 Hz. The plot in the top right corner shows the trajectory in MLat/MLT coordinates. The magenta line is the trajectory, the blue dots correspond to the times given in the plot in UT.

break frequency (panels d and e) and the integrated power within 1–2 Hz and 6–7 Hz from the same PSD. Panels g–i show the slopes, spectral break frequency if applicable and the integrated power between 1–2 Hz and 20–21 Hz for 1-min intervals from the B_y PSD, respectively.

The satellite encounters very little density fluctuations in both mid-latitude (MidLat) regions. This is linked with a single slope and little integrated power in the corresponding power spectra. One way to distinguish the auroral oval (AO) from the PC and MidLat regions is by looking at the FAC graph (panel b) and the B_y graph (panel c). When the satellite passes the AO, north of 67° MLat, the N_e power spectra (panels d and e) start being best

described by a double slope instead of a single slope and the integrated power (panel f) rises. Within the PC, recognizable by the region in between the strong fluctuations in the FAC and B_y, N_e shows several increases, for example, at 13:26 UT, which can be associated with polar cap patches. The strongest N_e fluctuations occur between 13:21 UT and 13:28 UT. After that, the N_e fluctuations diminish slightly. While the integrated power from the N_e PSD (panel f) clearly exhibits peaks within the AO during strong FAC fluctuations, a third peak can be seen within the PC. This third peak around 13:26–13:27 UT occurs simultaneously and could thus be linked to the polar cap patch at 13:27 UT. However, it should be mentioned that the two PSD at that time are described by a single fit rather than two fits as seen from the two blue circles. The slopes from the B_y PSD (panel g) are best described by a double slope throughout the majority of the pass, while the integrated power from the same PSD (panel i) is enhanced within the AO.

For the duration of the time interval chosen for the analysis we analyze 12,490 passes over the poles, roughly equally distributed over both hemispheres. This corresponds to about 400,000 power spectra for N_e and about the same amount for the B_y data.

In order to do a statistical approach, we bin the data into several regions between 50 and 90° MLat in 2° steps and between 0 and 24 hr MLT in 1 hr steps. If the satellites have several passes within a given region, leading to more than one data point within the bin, the mean of all data points within the bin is calculated for the graphs depicting the integrated power of N_e and B_y, as well as the ROTI data. For the slope probability plots we calculate the chance for a single slope by dividing the number of single slopes by the total number of passes within a bin. The double slope probability is calculated in a similar way. These two quantities are merged into a probability scale ranging from 100% single slope probability (SS probability) to 100% double slope probability (DS probability).

3. Results

We use all passes Swarm A and C made between October 2014 and December 2016 where N_e, B, and FAC data are available. Additionally, we use all passes between January 2020 and December 2022 with the same requirements. The data from the low activity timeframe (2020–2022) does not vary greatly from the high activity data (2014–2016). Additionally, the passes between 2020 and 2022 are limited by the 16 Hz N_e data which is only collected for short intervals within the given timeframe. Thus, this data can be found in Appendix A for comparison. Figure 3 shows slope probability and integrated power for high solar activity (2014–2016) obtained from the electron density PSD. The plot is divided into four seasons from spring to winter in column 1–4, respectively. The first two rows, rows a and b, show the slope probability and integrated power of the northern hemisphere (NH), respectively, while the two bottom rows, rows c and d, show the same quantities for the southern hemisphere (SH). The slope probability ranges from 100% DS probability (dark red) to 100% SS probability (dark blue). If it is equally likely to obtain a single or double slope in the corresponding bin, the bin is yellow.

Both the northern and southern hemisphere slope probability (rows a and c) show a seasonal dependency. In local summer the slope probability for a DS throughout the AO, which is typically found in around 70° MLat, and PC is close to one, especially in the PC. For both spring and autumn, the probability for a double slope is still very close to 1, however, compared to the summer, the probability in the AO becomes higher than in the PC. This ratio grows further during winter time, where the probability in the PC is nearly similar for a spectrum to exhibit a double slope as it is to exhibit a single slope. Note that the probability for a double slope stays high in the AO for all seasons. While a higher DS probability is found mostly throughout the AO and PC regions, the dayside MidLat below approximately 60° MLat shows a very high SS probability, which is also the only region where we consistently find a higher probability for a SS than a DS. In the night time below 60° MLat we rather encounter an equal slope probability. These findings hold true for both northern and southern hemisphere, though the contrast between summer and the other seasons seems to be more pronounced in the SH. Additionally, we find similar results for low solar activity (2020–2022), which can be seen in Appendix A, see Figure A1. Furthermore, the autumn season shows a higher double slope probability at lower latitudes for the midnight sector in comparison to the other seasons. Note that all seasons are local seasons, which means that the autumn data from the northern hemisphere corresponds to the same time frame as the spring data of the southern hemisphere. As both hemispheres show a higher double slope probability around midnight for lower latitudes in the autumn, this is not related to a small number of events leading to higher probabilities, but rather is to be related to the season itself.

Rows b and d show the integrated power between 1 and 2 Hz. Again, we find a seasonal dependency, though this time we find differences in the northern and southern hemisphere. In the NH the integrated power is more
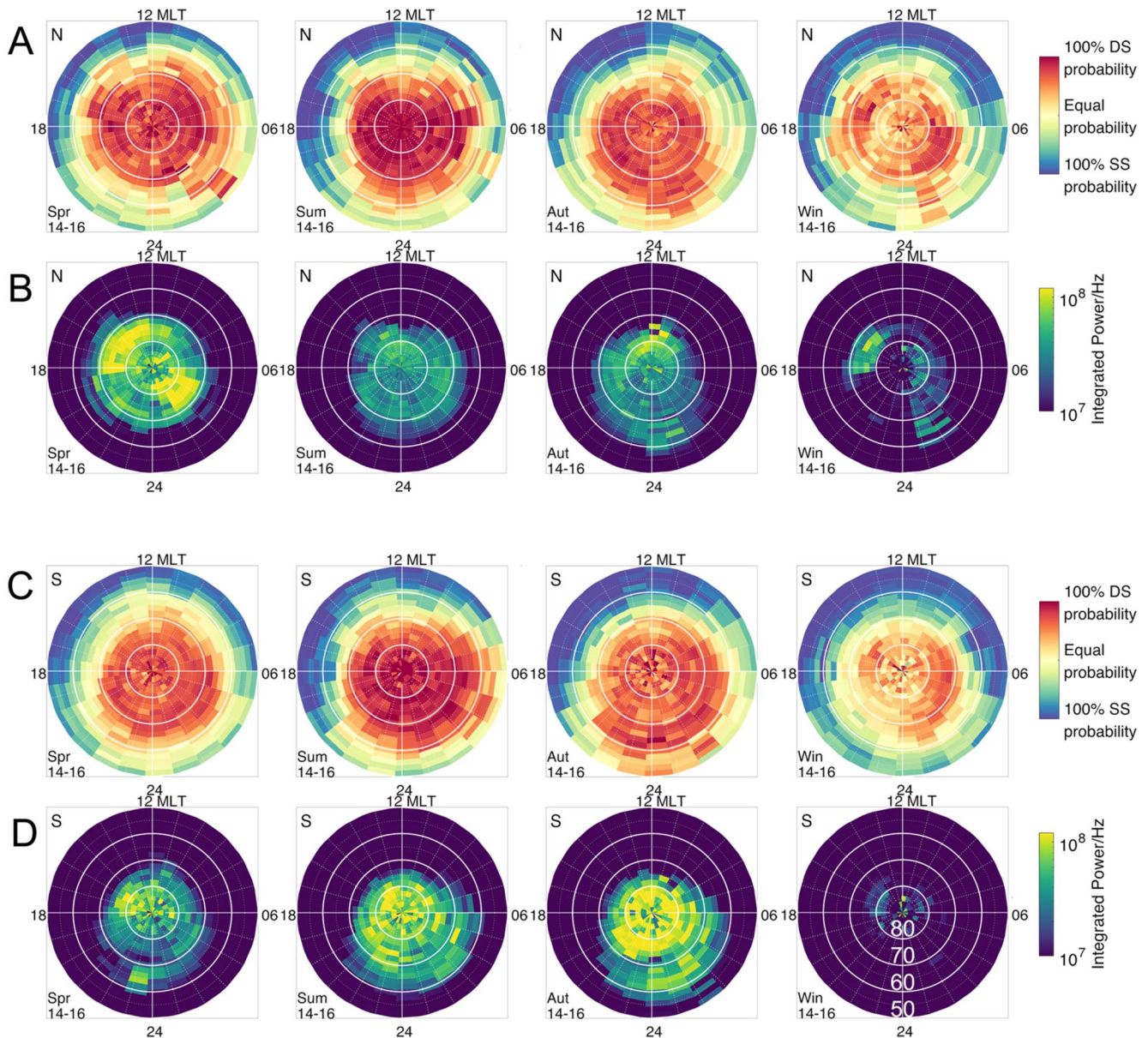
Figure 3. Slope probability and integrated power for the interval between 1 and 2 Hz obtained from the N_e PSD. The four columns contain the four seasons from spring to winter, while the four rows, rows (a–d), show the slope probability and integrated power for the northern hemisphere (rows a and b) and for the southern hemisphere (c and d) for high solar activity (years 2014–2016). All seasons are local seasons. The magnetic latitude is indicated on the bottom right plot.

pronounced around the spring and autumn equinoxes than the summer, with little integrated power throughout the winter. However, the SH has a higher integrated power in summer than spring, though autumn still exhibits the highest power. In both cases, the integrated power in local winter is significantly lower when compared to other seasons. This also holds true for low solar activity in Figures A1b and A1d. For the slope probability we obtain a lower probability for a double slope in the PC during autumn, spring and winter compared to summer, though the probability in the AO stays high. The integrated power, however, stays elevated in the PC compared to the AO, even if the overall power diminishes. Notable is also the high integrated power northward of 60° MLat around midnight during spring in the southern hemisphere (bottom left panel), which does not correspond with a higher probability for either a single or double slope. Generally, while both the double slope probability and integrated power are more pronounced throughout the AO and PC, a high integrated power is not necessarily followed by a higher double slope probability.

Another important aspect is the asymmetry between the hemispheres. The slope probability shows a high similarity for all seasons with high probabilities in the summer and diminishing probabilities for the equinoxes and winter for both high and low solar activity. However, the integrated power shows no such resemblances. Generally, the SH summer integrated power is enhanced in comparison to the other seasons, while in the northern hemisphere the integrated power around the equinoxes is more pronounced.

Figure 4 shows ROTI obtained from the IPIR data set, for the northern and southern hemispheres (row a and b, respectively). The four columns show the four seasons from spring to winter going from left to right. The northern hemisphere shows an elevated ROTI in the spring and autumn mainly in the night side auroral oval and between 70 and 80° MLat around noon. While the same areas are also enhanced during summer, the overall index is lower than around the equinoxes. Note, that the index in the NH polar cap is generally more enhanced than the index in the MidLat, though the largest enhancements are found within the AO. The southern hemisphere is generally more enhanced than the NH, though, similar to the electron density results, a difference during seasons can be observed. The local summer and autumn seasons are overall more enhanced than the other seasons, especially within the polar cap. During local spring, ROTI is mainly enhanced within the nightside auroral oval around midnight and northward of 70° MLat around noon. For both hemispheres local winter shows comparably low enhancement within all regions.

Figure 5 is displayed similar to Figure 3 and shows the slope probability and integrated power obtained from the PSD of the B_y component. The plot is divided into four seasons from spring to winter in column 1–4, respectively. The first two rows, rows a and b, show the slope probability and integrated power of the NH, respectively, while the two bottom rows, rows c and d, show the same quantities for the SH.

In both the northern and southern hemisphere the double slope probability (row a and c) is high in the AO and cusp region, typically found around noon and 75° MLat. Additionally, we find a higher double slope probability southward of 60° MLat on the nightside. While the dayside shows an equal probability for single and double slopes southward of 70° MLat for nearly all plots, there is a higher DS probability on the dayside around 50° MLat. Generally, it is either likely that we can find an equal probability or a higher probability for double slopes throughout all plots, only very little bins show a higher probability for a single slope, and if so, the bins are either located on the dayside, in the PC or directly southward of the PC around midnight. This holds true, again, for the slope probabilities during low activity, see Figure A2 in Appendix A. However, the single slope probability is still dominant in few bins. Moreover, both autumn graphs (A and C, third plot) show a stronger double slope probability between 60° MLat and 70° MLat during midnight.

The integrated power between 1 and 2 Hz (row b and d) is also most elevated in the AO throughout all plots both for high and low activity. While most of the auroral oval exhibits a more or less uniform elevated integrated power, there is higher powers found around 75° MLat around magnetic noon, thus in the cusp, for several of the plots. While the slope probability shows a strong double slope probability within the midnight section below 60° MLat, this is not the case for the integrated power.

4. Discussion

In this study we utilize over 2 years of in situ measurements from Swarm A and C data in order to investigate a connection between irregularities in the B_y component and strong electron density fluctuations in the polar ionosphere. Additionally, we use ROTI data from the IPIR data set.

We compare the slope probability and integrated power between 1 and 2 Hz of the N_e PSD in the NH and SH for solar maximum. Both quantities show a seasonal dependency, though not for the same seasons. The slope probability varies with solar EUV radiation, meaning that we find the highest probability for a double slope to describe a power spectrum in local summer months. Close to the equinoxes the probability for a DS becomes less, especially in the polar cap. This tendency becomes even stronger during winter months, where the DS probability is roughly equal to a SS probability for most parts within the PC. These results are consistent with Ivarsen et al. (2021). They have linked the existence of DS to the influence of the SZA, showing a higher DS probability with lower SZA, presenting evidence for a dependency of N_e irregularities in the polar cap on solar EUV radiation. A higher solar EUV radiation leads to an increase of conductivity in the E-region, which consequently leads to a faster decay of plasma structures in the F-region due to the coupling between both regions (Buschmann et al., 2023; Ivarsen et al., 2019, 2023; M. C. Kelley et al., 1982). The increased decay of plasma structuring
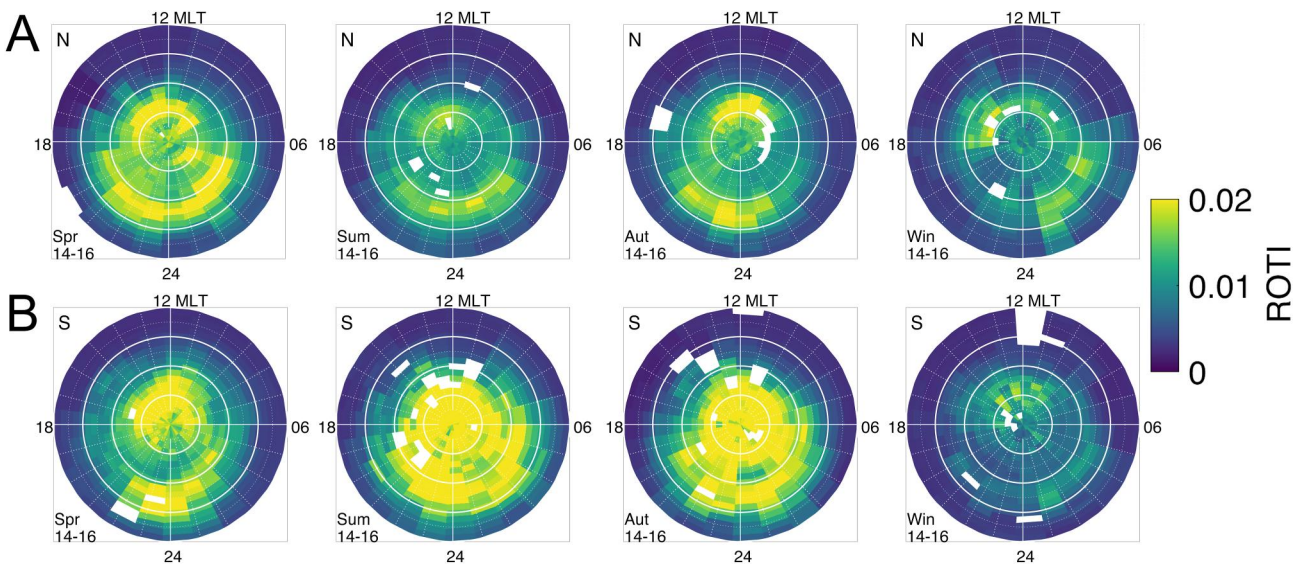
Figure 4. Rate of change of TEC Index (ROTI). The four columns contain the four seasons from spring to winter, while the two rows, rows (a and b), show the ROTI for the northern hemisphere and southern hemisphere (rows a and b, respectively) for high solar activity (years 2014–2016). All seasons are local seasons. The magnetic latitude is indicated on the bottom right plot.

together with a generally higher N_e due to solar EUV radiation leads to a PSD with higher values on large scales and lower values on small scales, thus increasing the chance to for two slopes to the corresponding spectra.

At this point it is worth mentioning that a quantity of PSD equator-ward of the AO is shallowing out, meaning the second, high-frequency slope is very flat compared to the first slope. This mainly happens in regions where N_e is smooth and unstructured. When looking at the slopes of the PSD in a turbulence context, a shallow slope is associated with an energy input in these frequencies. The algorithm that is used for slope detection, however, labels these spectra as single slopes, as the condition $p_2 - p_1 \geq 0.8$ is not met.

As mentioned within the methodology section of this study, the algorithm is only able to detect a slope in a frequency range between 0.19 and 7 Hz, which corresponds to scale sizes of approximately 1.1–40 km. Sounding rocket data have shown that breakpoints can occur on a variety of scales ranging up to 100 Hz. A variety of different frequencies may indicate a cascade from very large scales within the solar wind down to centimeter scale sizes found within the ionosphere with spectral steepening and breakpoints at several different scales stemming from different mechanisms. The 16 Hz N_e data limits the observable range up to 8 Hz corresponding to the Nyquist frequency. The spectral breaks observed within this study are occurring on kilometer scales and can thus be an indication of a redistribution of energy due to the GDI, which operates on these scale sizes, especially on the edges of polar cap patches.

The integrated power for the N_e PSD show seasonal dependencies for the NH and SH. The northern hemisphere generally shows a higher power around the equinoxes, while the southern hemisphere additionally exhibits elevated power in local summer. Generally, while the slope probability in the NH and SH are very similar, the integrated power shows no such similarity between the hemispheres and seasons. This suggests that the energy deposited in kilometer-scale structures is not necessarily linked to steepening of the PSD. The higher integrated power obtained from the N_e PSD around the equinoxes may be explained due to the tilt of the Earth's axis and the additionally slanted magnetic field, leading to a better alignment between the Earth's magnetic field and that of the solar wind. Generally, the seasonal variation of geomagnetic storms has been ascribed to both axial and equinoctial phenomena, alongside the Russell-McPherron effect (Cortie, 1912; Echer et al., 2011; Gonzalez et al., 1994; Russell & McPherron, 1973). The elevated occurrence of geomagnetic storms and the accompanying precipitating particles can then lead to a higher deposition of energy into lower frequencies, as analyzed here, around the equinoxes. An increased deposition of energy into low frequencies during particle precipitation has as well been described in Buschmann et al. (2023), who have analyzed the impact of particle precipitation on plasma structuring within different scales with sounding rockets. The study found an increase in kilometer-sized scales within the cusp aurora, which was broken down to smaller structures poleward of the cusp. The enhanced PSD in the southern
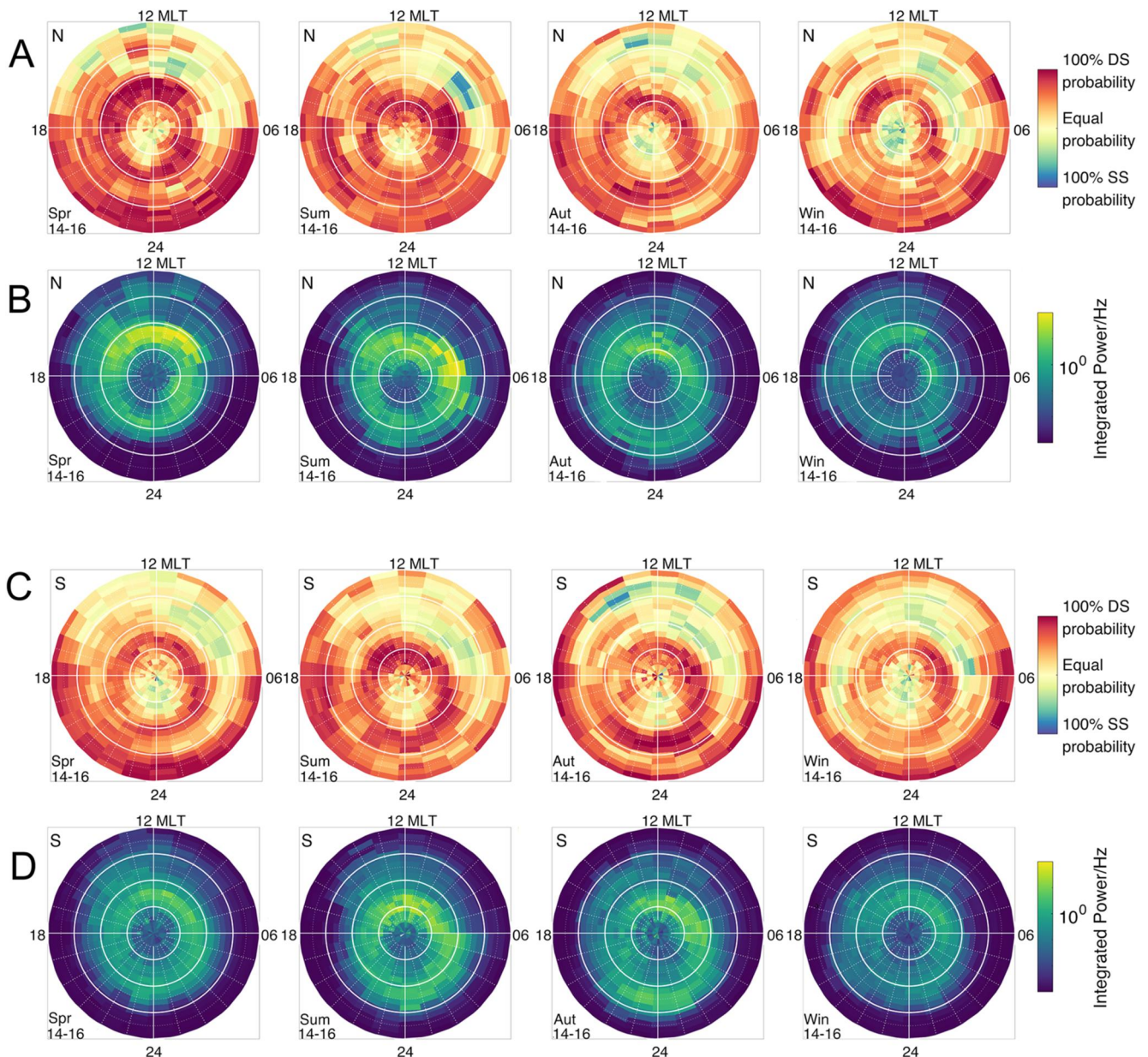
Figure 5. Slope probability and integrated power for the interval between 1 and 2 Hz obtained from the PSD of the B_y component. The four columns contain the four seasons from spring to winter, while the four rows, rows (a–d), show the slope probability and integrated power for the northern hemisphere (rows a and b) and for the southern hemisphere (c and d) for high solar activity (years 2014–2016). All seasons are local seasons. The magnetic latitude is indicated on the bottom right plot.

hemisphere within the summer months could be caused by the additional offset of the Earth's magnetic field in the SH. The magnetic pole in the SH is more than 8.5° farther from the geographic pole in the SH when compared to the NH. This results in higher illumination in the southern polar region. Convection can then lead to a higher structuring within the summer month in the SH (Coley & Heelis, 1998; Laundal et al., 2017; Noja et al., 2013). In local winter, both the NH and SH integrated power show the lowest values throughout the seasons. In addition to the 1–2 Hz interval we analyze data in between 0.1–0.6 Hz and 6–7 Hz, corresponding to scale sizes between about 10 and 80 km and of about 1 km, respectively. Both data sets show similar trends to the analysis of the 1–2 Hz interval, indicating consistent results throughout the scale sizes. As the plots yield similar results as the 1–2 Hz plots displayed within this work, we decided not to include them but rather give the short description above.

In order to get a better picture of the structuring of N_e within the polar regions, we also analyze the ROTI data within the same time-frame as the PSD analysis. The overall seasonal variation of the ROTI data aligns with the

seasonal variation that we found within the integrated power of the N_e PSD. Additionally, the interhemispheric variation that is seen within the integrated power from the N_e PSD can also be seen within this data set and is consistent with Jin and Xiong (2020). Generally, the majority of the enhanced ROTI locations also match the integrated power. However, ROTI is much more elevated within the cusp region and nightside AO in the northern hemisphere, while the southern hemisphere shows an additional pronunciation from the cusp into the nightside until the central polar cap, with a small region that exhibits a lower ROTI in the nightside PC. Similar to the integrated power, ROTI also shows a clear distinction between the NH and SH. The low ROTI in winter and higher ROTI values around the equinoxes is consistent with results in Jin et al. (2019). The integrated power is derived from the 16 Hz in situ N_e data and thus gives momentary information in the vicinity of the satellite. Additionally, we gain information on the amplitude of fluctuations within a certain scale size (here within 1– 2 Hz). ROTI data, on the other hand, gives insight about the structuring of the plasma for a wider ionospheric area, as the data is obtained from GNSS signals.

In addition to the PSD analysis of N_e, we also analyze the slope probability and integrated power between 1 and 2 Hz of B_y. Both the occurrence rate for a double slope and the integrated power show elevated values within the auroral oval and within the cusp. Additionally, it is more likely for a double slope to occur below 60° MLat, especially during nighttime, however, there is no elevation within the integrated power. As B_y in this study is used instead of the FAC data, the signal within mid-latitudes is usually low, which may lead to a very low signal within the PSD. Furthermore, as seen in Figure 2, the breakpoints in the nightside mid-latitude region are very high and close to the Nyquist frequency for the B_y PSD. This adds additional uncertainty for these spectra. Thus, the double slope probability in these regions should be assessed with caution and may likely be a result of noise.

Generally, the residual magnetic field fluctuations show an integrated power enhancement in a circle around the pole, similar to the FAC data, see Figure A3. In addition, the highest values are found in the morning sector and the cusp for all seasons and both hemispheres, indicating dayside precipitation. An increased integrated power within these scales indicates an enhancement in Poynting flux. The Poynting flux gives a measure of electromagnetic energy moving between the magnetosphere and the ionosphere through the FAC. Generally, the Poynting Flux can be divided into large scale variations along the R1/R2 FAC system (Iijima & Potemra, 1976), or into variations on small scales, usually below 10 km, where Alfvénic energy plays a large role (Knudsen et al., 1992). The integrated power we analyze within this study corresponds to scale sizes of a few kilometers, falling into the range below 10 km. This indicates that the increased integrated power we obtain gives a measure on the downward Poynting flux dominated by Alfvénic energy. In recent years, studies with the Swarm satellites have been conducted to present maps of the Poynting flux in the northern and southern hemisphere (Billett et al., 2022; Ivarsen et al., 2020). The climatology we present of the B_y integrated power maps onto the Poynting flux within these studies adequately with an overall increase in Poynting flux in a circular shape around the magnetic pole and a further increase within the cusp.

It has also been shown that Alfvén waves contribute significantly to the energy input into the auroral acceleration region. The applied energy can then trigger amongst others particle precipitation into the ionosphere and thus formation of aurora (Angelopoulos et al., 2002; Chaston, 2006; Keiling, 2009; Wygant et al., 2000).

The enhancements within B_y integrated power in the cusp are also co-located with the strong ROTI enhancements as seen in Figure 4. This agrees with previous results that show how auroral dynamics within the cusp can be related to irregularities leading to high values of phase scintillations indices based on GNSS signals (Clausen et al., 2016; Jin et al., 2015, 2017). This also agrees with Fæhn Follestad et al. (2020), who showed that filamentary FACs are co-located with high phase scintillation indices in the cusp.

5. Conclusion

We present analysis of more than 2 years of data from the 16 Hz electron density, the 50 Hz magnetic field and ROTI data from the IPIR data set from Swarm A and C. Additionally, we use 3 years of a complementary data set from Swarm A and C for a time frame around solar minimum for discussion. We have been able to find new results and give new insights, as well as confirm previously found results from different studies with our methods. The probability for a DS within the N_e PSD follows a seasonal variation that changes with EUV radiation within the PC. For both hemispheres we observe the highest DS probability in local summer. Both equinoxes show lower probability, while the winter season shows the lowest probability. The DS probability within the AO is constantly

high and is thus independent of solar EUV and rather depends on auroral dynamics. Higher solar EUV photo-ionization causes an upturn in E-region conductivity leading to a faster decay of structures in F-region plasma. With an overall increase in N_e within summer due to solar EUV radiation, this increases the DS probability in the summer, but overall indicates less small-scale structuring in the polar cap in the summer months. The integrated power within the 1–2 Hz frequency interval also shows a seasonal variation, however, the variation does not correlate to solar EUV radiation, but rather has its strongest values around the equinoxes and the lowest values in winter. Additionally, while the DS probability shows little difference between the hemispheres, the integrated power shows much higher variability, especially within local summer months. This is likely attributed to the large offset of the magnetic pole in the southern hemisphere. The ROTI values show a similar variation as the integrated power obtained from N_e. However, while the integrated power, especially in the NH, shows a similar elevation for the AO and PC, the ROTI values show higher elevation within the midnight auroral oval and within the cusp. The overall seasonal variation of ROTI has been seen before, however, this study gives a seasonal climatology of the results and thus expands on the already existing studies. While the integrated power generally gives a measure of the strength of fluctuations and structuring, similar to ROTI, the results are limited to certain spatial scales. The integrated power within both hemispheres is mainly enhanced within the PC and AO, though varying in strength. Generally, ROTI shows enhancements within the same regions, however, the midnight AO and the cusp show further heightened values, thus indicating higher structuring within these regions. We also find higher values of the integrated power of B_y within the cusp, co-located with the ROTI data. The enhancements within the B_y integrated power also match with previous studies which analyzed the Poynting flux from the Swarm satellite. The enhancements within the cusp correspond to spatial scales below 10 km and are thus on scales where Alfvénic energy plays a large role. The increased values within the cusp may thus be linked to an increase in precipitating particles into the cusp.

The B_y DS probability, as well as the N_e SS probability are enhanced within mid-latitudes. The low signals for both N_e and B_y in mid-latitudes can lead to uncertainty in the assessment of the spectral index due to the low signal in the PSD. Furthermore, N_e may exhibit a shallow second slope in regions of smooth or unstructured plasma, as it is found within mid-latitudes. As the condition for the algorithm of $p_2 - p_1 \geq 0.8$ is not met, these spectra may be labeled as a single slope, even though turbulence theory associates a more shallow slope with an input of energy. Additionally, we encounter breakpoints for the B_y PSD close to the Nyquist frequency we obtain for the 50 Hz data, which adds uncertainty to this data set within mid-latitudes. The data within this region should thus be viewed with caution.

This study has implications for a better understanding of plasma structuring in the ionosphere and models for space weather effects. Structures in the electron density on scales assessed in this study of between a few hundred and a few kilometers have been shown to lead to elevated phase scintillations indices, σ_Φ, calculated for incoming GNSS signals (Jin et al., 2017; Kintner et al., 2007). Additionally, due to the turbulent cascade and energy redistribution within the ionosphere, the existence of kilometer-sized structures can sometimes be directly linked to the formation of sub-kilometer sized structures (Hamza et al., 2024). Under these conditions, when sub-kilometer sized structures are present, diffractive effects can lead to GNSS scintillations of stochastic nature which can be observed as elevated scintillation indices. This effect is mostly pronounced in the cusp region (Meziane et al., 2020). However, we note that very often the large scale structuring in TEC leads to elevated σ_Φ, but not amplitude scintillations (Enengl et al., 2024; Zheng et al., 2022). This is often the case in regions close to the auroral oval. Thus, elevated ROTI can often be an indication of large scale structuring, which can lead to problems such as loss-of-lock. A better understanding of plasma structuring and the redistribution of energy can thus aid in improving forecasting and modeling of space weather effects.

To summarize, we can present the main results of this paper as follows:

- The probability to obtain a double slope in the N_e PSD shows a seasonal dependency on the influence of solar-EUV and little variation between the northern and southern hemisphere. The integrated power within the frequency interval of 1–2 Hz from the same PSD shows a seasonal dependency with higher power during the equinoxes and a strong interhemispheric variation. A connection between the two quantities can thus not be shown within the scope of this study.
- ROTI data shows similar behavior to the integrated power from the N_e PSD but shows larger enhancements within the cusp and nightside auroral oval, which may indicate different drivers for instabilities within these regions.

- The strongest fluctuations within B_y are found within the cusp for all seasons and both hemispheres. These enhancements can be linked to an increase in downward Poynting flux on scales below 10 km which corresponds to an increase in Alfvén energy. The enhancements in B_y are additionally co-located with strong ROTI values.

In order to achieve a better picture of the redistribution of irregularities in the polar ionosphere, it would be beneficial in the future to use data with a higher sampling rate in order to map the energy contained over a large range of scales.

Appendix A: Additional Data

Complimentary data sets from January 2020 to December 2022 have been analyzed for comparison. Figure A1 shows slope probability and integrated power for low solar activity (2020–2022) obtained from the electron
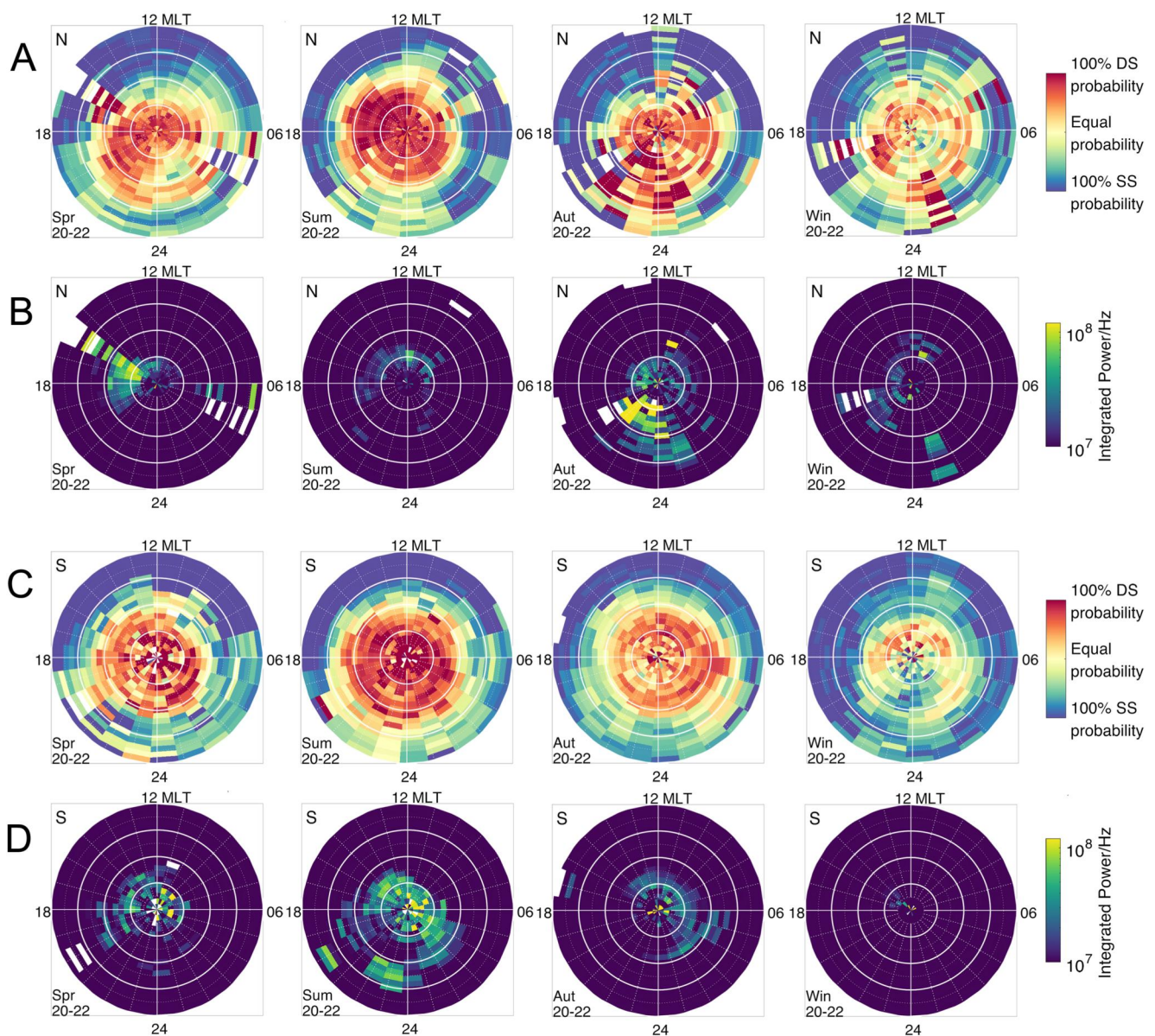

Figure A1. Slope probability and integrated power for the interval between 1 and 2 Hz obtained from the N_e PSD. The four columns contain the four seasons from spring to winter, while the four rows, rows (a–d), show the slope probability and integrated power for the northern hemisphere (rows a and b) and for the southern hemisphere (c and d) for low solar activity (years 2020–2022).
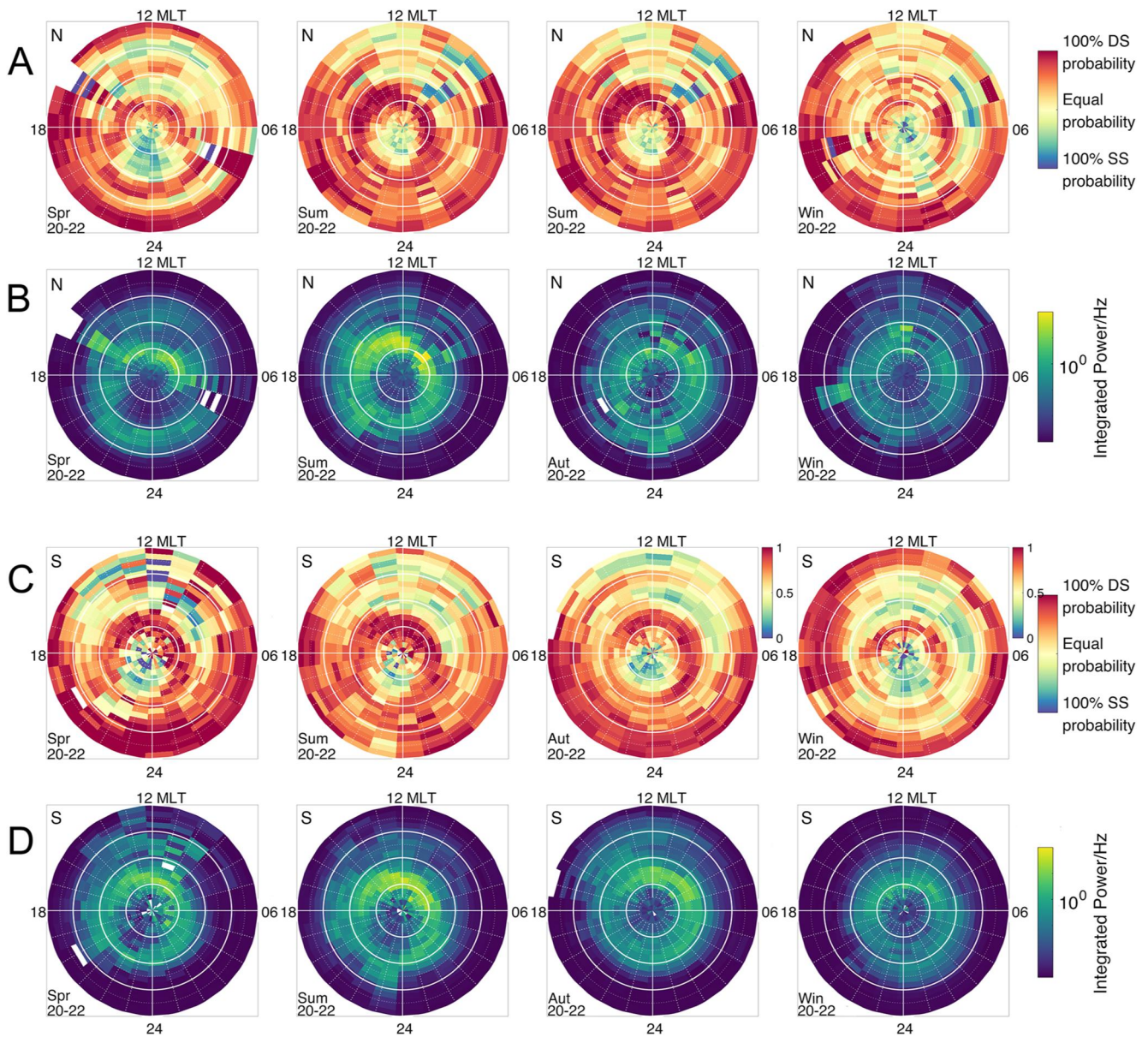
Figure A2. Slope probability and integrated power for the interval between 1 and 2 Hz obtained from the B_y PSD. The four columns contain the four seasons from spring to winter, while the four rows, rows (a–d), show the slope probability and integrated power for the northern hemisphere (rows a and b) and for the southern hemisphere (c and d) for low solar activity (years 2020–2022).

density PSD. The plot is divided into four seasons from spring to winter in column 1–4, respectively. The first two rows, rows a and b, show the slope probability and integrated power of the northern hemisphere (NH), respectively, while the two bottom rows, rows c and d, show the same quantities for the southern hemisphere (SH). The slope probability ranges from 100% DS probability (dark red) to 100% SS probability (dark blue). If it is equally likely to obtain a single or double slope in the corresponding bin, the bin is yellow. Figure A2 shows the same quantities obtained from the B_y PSD. Figure A3 shows the 1 Hz FAC data. The two top rows, rows a and b, show the FAC in the northern hemisphere for high solar activity (row a) and low solar activity (row b), while the two bottom rows, rows c and d, show the FAC in the southern hemisphere for high solar activity (row c) and for low solar activity (row d).
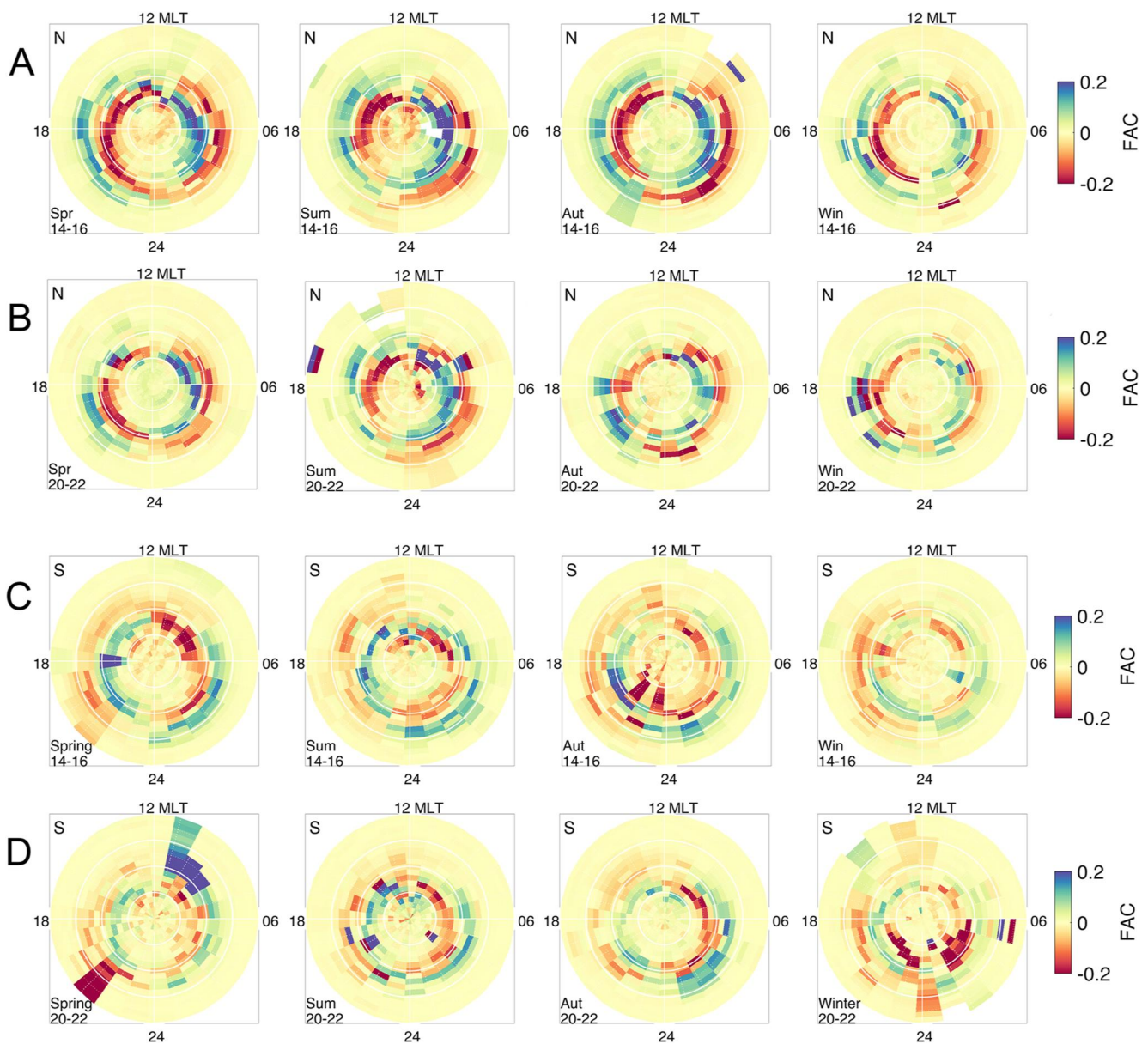
Figure A3. Field aligned current from the 1 Hz Swarm FAC data. The four columns contain the four seasons from spring to winter, while the four rows, rows (a–d), show the FAC for the northern hemisphere (rows a and b) for high solar activity (row a) and low solar activity (row b), and for the southern hemisphere (c and d) for high solar activity (row c) and low solar activity (row d).

Data Availability Statement

The European Space Agency's Swarm data, including the IPIR product, can be accessed at https://swarm-diss.eo.esa.int. Information about the Swarm data can be taken from the Swarm Data Handbook in ESA (n.d.), https://swarmhandbook.earth.esa.int.

References

AD, R. (1995). Ionospheric electrodynamics using magnetic apex coordinates. *Journal of geomagnetism and geoelectricity*, *47*(2), 191–212. https://doi.org/10.5636/jgg.47.191

Angelopoulos, V., Chapman, J., Mozer, F., Scudder, J., Russell, C., Tsuruda, K., et al. (2002). Plasma sheet electromagnetic power generation and its dissipation along auroral field lines. *Journal of Geophysical Research*, *107*(A8), SMP–14. https://doi.org/10.1029/2001JA900136

Basu, B., & Coppi, B. (1988). Fluctuations associated with sheared velocity regions near auroral arcs. *Geophysical research letters*, *15*(5), 417–420. https://doi.org/10.1029/gl015i005p00417

Basu, S., Basu, S., MacKenzie, E., Coley, W., Sharber, J., & Hoegy, W. (1990). Plasma structuring by the gradient drift instability at high latitudes and comparison with velocity shear driven processes. *Journal of Geophysical Research*, *95*(A6), 7799–7818. https://doi.org/10.1029/JA095iA06p07799

Billett, D. D., McWilliams, K. A., Pakhotin, I. P., Burchill, J. K., Knudsen, D. J., & Martin, C. J. (2022). High-resolution Poynting flux statistics from the swarm mission: How much is being underestimated at larger scales? *Journal of Geophysical Research: Space Physics*, *127*(7), e2022JA030573. https://doi.org/10.1029/2022JA030573

Buschmann, L. M., Spicher, A., Clausen, L. B., Marholm, S., & Miloch, W. J. (2023). The role of particle precipitation at different altitudes by in-situ measurements. *Journal of Space Weather and Space Climate*, *13*, 1. https://doi.org/10.1051/swsc/2023012

Carlson, H. C. (2012). Sharpening our thinking about polar cap ionospheric patch morphology, research, and mitigation techniques. *Radio Science*, *47*(4). https://doi.org/10.1029/2011RS004946

Carlson, H. C., Pedersen, T., Basu, S., Keskinen, M., & Moen, J. (2007). Case for a new process, not mechanism, for cusp irregularity production. *Journal of Geophysical Research*, *112*(A11), A11304. https://doi.org/10.1029/2007JA012384

Carrano, C. S., Groves, K. M., McNeil, W. J., & Doherty, P. H. (2013). Direct measurement of the residual in the ionosphere-free linear combination during scintillation. In *Proceedings of the 2013 international technical meeting of the institute of navigation* (pp. 585–596).

Chartier, A. T., Huba, J., & Mitchell, C. N. (2019). On the annual asymmetry of high-latitude sporadic F. *Space Weather*, *17*(11), 1618–1626. https://doi.org/10.1029/2019SW002305

Chartier, A. T., Mitchell, C. N., & Miller, E. S. (2018). Annual occurrence rates of ionospheric polar cap patches observed using Swarm. *Journal of Geophysical Research: Space Physics*, *123*(3), 2327–2335. https://doi.org/10.1002/2017JA024811

Chaston, C. (2006). ULF waves and auroral electrons. *Magnetospheric ULF waves: Synthesis and new directions*, *169*, 239–257. https://doi.org/10.1029/169GM16

Clausen, L., Moen, J., Hosokawa, K., & Holmes, J. (2016). GPS scintillations in the high latitudes during periods of dayside and nightside reconnection. *Journal of Geophysical Research: Space Physics*, *121*(4), 3293–3309. https://doi.org/10.1002/2015JA022199

Coley, W., & Heelis, R. (1998). Seasonal and universal time distribution of patches in the northern and southern polar caps. *Journal of Geophysical Research*, *103*(A12), 29229–29237. https://doi.org/10.1029/1998JA900005

Cortie, A. (1912). Sun-spots and terrestrial magnetic phenomena, 1898-1911. *Monthly Notices of the Royal Astronomical Society*, *73*(1), 52–60. https://doi.org/10.1093/mnras/73.1.52

Crowley, G., Schoendorf, J., Roble, R. G., & Marcos, F. A. (1996). Cellular structures in the high-latitude thermosphere. *Journal of Geophysical Research*, *101*(A1), 211–223. https://doi.org/10.1029/95JA02584

David, M., Sojka, J. J., Schunk, R. W., & Coster, A. J. (2019). Hemispherical shifted symmetry in polar cap patch occurrence: A survey of GPS TEC maps from 2015–2018. *Geophysical Research Letters*, *46*(19), 10726–10734. https://doi.org/10.1029/2019GL083952

De Franceschi, G., Spogli, L., Alfonsi, L., Romano, V., Cesaroni, C., & Hunstad, I. (2019). The ionospheric irregularities climatology over Svalbard from solar cycle 23. *Scientific reports*, *9*(1), 9232. https://doi.org/10.1038/s41598-019-44829-5

D'Errico, J. (2017). SLM—Shape language modeling. (MATLAB File Exchange). Retrieved from https://se.mathworks.com/matlabcentral/fileexchange/24443%2Dslm%2Dshape%2Dlanguage%2Dmodeling

Di Mare, F., Spicher, A., Clausen, L. B. N., Miloch, W. J., & Moen, J. I. (2021). Turbulence and intermittency in the winter cusp ionosphere studied with the ICI sounding rockets. *Journal of Geophysical Research: Space Physics*, *126*(8), e2021JA029150. https://doi.org/10.1029/2021JA029150

Echer, E., Gonzalez, W., & Tsurutani, B. (2011). Statistical studies of geomagnetic storms with peak Dst—50 nT from 1957 to 2008. *Journal of Atmospheric and Solar-Terrestrial Physics*, *73*(11–12), 1454–1459. https://doi.org/10.1016/j.jastp.2011.04.021

Emmert, J., Richmond, A., & Drob, D. (2010). A computationally compact representation of magnetic-apex and quasi-dipole coordinates with smooth base vectors. *Journal of Geophysical Research*, *115*(A8), A08322. https://doi.org/10.1029/2010JA015326

Enengl, F., Spogli, L., Kotova, D., Jin, Y., Oksavik, K., Partamies, N., & Miloch, W. (2024). Investigation of ionospheric small-scale plasma structures associated with particle precipitation. *Space Weather*, *22*(1), e2023SW003605. https://doi.org/10.1029/2023sw003605

ESA. (n.d.). Swarm data handbook. Retrieved from https://swarmhandbook.earth.esa.int

Fæhn Follestad, A., Herlingshaw, K., Ghadjari, H., Knudsen, D. J., McWilliams, K. A., Moen, J. I., et al. (2020). Dayside field-aligned current impacts on ionospheric irregularities. *Geophysical Research Letters*, *47*(11), e2019GL086722. https://doi.org/10.1029/2019GL086722

Friis-Christensen, E., Lühr, H., & Hulot, G. (2006). Swarm: A constellation to study the Earth's magnetic field. *Earth, Planets and Space*, *58*(4), 351–358. https://doi.org/10.1186/BF03351933

Friis-Christensen, E., Lühr, H., Knudsen, D., & Haagmans, R. (2008). Swarm–an Earth observation mission investigating geospace. *Advances in Space Research*, *41*(1), 210–216. https://doi.org/10.1016/j.asr.2006.10.008

Frisch, U., & Kolmogorov, A. N. (1995). *Turbulence: The legacy of an Kolmogorov*. Cambridge University Press.

Ghobadi, H., Spogli, L., Alfonsi, L., Cesaroni, C., Cicone, A., Linty, N., et al. (2020). Disentangling ionospheric refraction and diffraction effects in GNSS raw phase through fast iterative filtering technique. *GPS Solutions*, *24*(3), 85. https://doi.org/10.1007/s10291-020-01001-1

Gonzalez, W., Joselyn, J.-A., Kamide, Y., Kroehl, H. W., Rostoker, G., Tsurutani, B. T., & Vasyliunas, V. (1994). What is a geomagnetic storm? *Journal of Geophysical Research*, *99*(A4), 5771–5792. https://doi.org/10.1029/93JA02867

Hamza, A. M., Song, K., Meziane, K., & Jayachandran, P. (2024). Two-component phase scintillation spectra in the auroral region: Observations and model. *Journal of Geophysical Research: Space Physics*, *129*(1), e2023JA031998. https://doi.org/10.1029/2023ja031998

Hosokawa, K., Taguchi, S., Ogawa, Y., & Sakai, J. (2013). Two-dimensional direct imaging of structuring of polar cap patches. *Journal of Geophysical Research: Space Physics*, *118*(10), 6536–6543. https://doi.org/10.1002/jgra.50577

Hysell, D., Kelley, M., Swartz, W., Pfaff, R., & Swenson, C. (1994). Steepened structures in equatorial spread F: 1. New observations. *Journal of Geophysical Research*, *99*(A5), 8827–8840. https://doi.org/10.1029/93JA02961

Iijima, T., & Potemra, T. A. (1976). The amplitude distribution of field-aligned currents at northern high latitudes observed by triad. *Journal of Geophysical Research*, *81*(13), 2165–2174. https://doi.org/10.1029/JA081i013p02165

Ivarsen, M. F., Jin, Y., Spicher, A., & Clausen, L. B. (2019). Direct evidence for the dissipation of small-scale ionospheric plasma structures by a conductive e region. *Journal of Geophysical Research: Space Physics*, *124*(4), 2935–2942. https://doi.org/10.1029/2019JA026500

Ivarsen, M. F., Park, J., Kwak, Y.-S., Jin, Y., Knudsen, D. J., & Clausen, L. B. (2020). Observational evidence for the role of hall conductance in Alfvén wave reflection. *Journal of Geophysical Research: Space Physics*, *125*(12), e2020JA028119. https://doi.org/10.1029/2020JA028119

Ivarsen, M. F., St-Maurice, J.-P., Hussey, G., Spicher, A., Jin, Y., Lozinsky, A., et al. (2023). Measuring small-scale plasma irregularities in the high-latitude E-and F-regions simultaneously. *Scientific Reports*, *13*(1), 11579. https://doi.org/10.1038/s41598-023-38777-4

Ivarsen, M. F., St-Maurice, J.-P., Jin, Y., Park, J., Miloch, W., Spicher, A., et al. (2021). Steepening plasma density spectra in the ionosphere: The crucial role played by a strong E-region. *Journal of Geophysical Research: Space Physics*, *126*(8), e2021JA029401. https://doi.org/10.1029/2021JA029401

Jahn, J.-M., & LaBelle, J. (1998). Rocket measurements of high-altitude spread F irregularities at the magnetic dip equator. *Journal of Geophysical Research*, *103*(A10), 23427–23441. https://doi.org/10.1029/97JA02636

Jin, Y., Kotova, D., Xiong, C., Brask, S. M., Clausen, L. B., Kervalishvili, G., et al. (2022). Ionospheric plasma irregularities-IPIR-data product based on data from the Swarm satellites. *Journal of Geophysical Research: Space Physics*, *127*(4), e2021JA030183. https://doi.org/10.1029/2021JA030183

Jin, Y., Moen, J. I., & Miloch, W. J. (2014). GPS scintillation effects associated with polar cap patches and substorm auroral activity: Direct comparison. *Journal of Space Weather and Space Climate*, *4*, A23. https://doi.org/10.1051/swsc/2014019

Jin, Y., Moen, J. I., & Miloch, W. J. (2015). On the collocation of the cusp aurora and the GPS phase scintillation: A statistical study. *Journal of Geophysical Research: Space Physics*, *120*(10), 9176–9191. https://doi.org/10.1002/2015JA021449

Jin, Y., Moen, J. I., Oksavik, K., Spicher, A., Clausen, L. B., & Miloch, W. J. (2017). GPS scintillations associated with cusp dynamics and polar cap patches. *Journal of Space Weather and Space Climate*, *7*, A23. https://doi.org/10.1051/swsc/2017022

Jin, Y., Spicher, A., Xiong, C., Clausen, L. B., Kervalishvili, G., Stolle, C., & Miloch, W. J. (2019). Ionospheric plasma irregularities characterized by the Swarm satellites: Statistics at high latitudes. *Journal of Geophysical Research: Space Physics*, *124*(2), 1262–1282. https://doi.org/10.1029/2018JA026063

Jin, Y., & Xiong, C. (2020). Interhemispheric asymmetry of large-scale electron density gradients in the polar cap ionosphere: UT and seasonal variations. *Journal of Geophysical Research: Space Physics*, *125*(2), e2019JA027601. https://doi.org/10.1029/2019JA027601

Kagawa, A., Hosokawa, K., Ogawa, Y., Ebihara, Y., & Kadokura, A. (2021). Occurrence distribution of polar cap patches: Dependences on UT, season and hemisphere. *Journal of Geophysical Research: Space Physics*, *126*(1), e2020JA028538. https://doi.org/10.1029/2020JA028538

Keiling, A. (2009). Alfvén waves and their roles in the dynamics of the Earth's magnetotail: A review. *Space Science Reviews*, *142*(1–4), 73–156. https://doi.org/10.1007/s11214-008-9463-8

Kelley, M., Pfaff, R., Baker, K., Ulwick, J., Livingston, R., Rino, C., & Tsunoda, R. (1982). Simultaneous rocket probe and radar measurements of equatorial spread F—Transitional and short wavelength results. *Journal of Geophysical Research*, *87*(A3), 1575–1588. https://doi.org/10.1029/JA087iA03p01575

Kelley, M. C., Vickrey, J. F., Carlson, C., & Torbert, R. (1982). On the origin and spatial extent of high-latitude F region irregularities. *Journal of Geophysical Research*, *87*(A6), 4469–4475. https://doi.org/10.1029/JA087iA06p04469

Keskinen, M., & Huba, J. (1990). Nonlinear evolution of high-latitude ionospheric interchange instabilities with scale-size-dependent magnetospheric coupling. *Journal of Geophysical Research*, *95*(A9), 15157–15166. https://doi.org/10.1029/ja095ia09p15157

Keskinen, M. J., & Ossakow, S. (1983). Theories of high-latitude ionospheric irregularities: A review. *Radio science*, *18*(06), 1077–1091. https://doi.org/10.1029/rs018i006p01077

Kintner, P. M., Ledvina, B. M., & De Paula, E. (2007). GPS and ionospheric scintillations. *Space weather*, *5*(9). https://doi.org/10.1029/2006SW000260

Kintner, P. M., & Seyler, C. E. (1985). The status of observations and theory of high latitude ionospheric and magnetospheric plasma turbulence. *Space science reviews*, *41*(1), 91–129. https://doi.org/10.1007/bf00241347

Knudsen, D., Kelley, M., & Vickrey, J. (1992). Alfvén waves in the auroral ionosphere: A numerical model compared with measurements. *Journal of Geophysical Research*, *97*(A1), 77–90. https://doi.org/10.1029/91JA02300

LaBelle, J., Kelley, M., & Seyler, C. (1986). An analysis of the role of drift waves in equatorial spread F. *Journal of Geophysical Research*, *91*(A5), 5513–5525. https://doi.org/10.1029/JA091iA05p05513

Laundal, K. M., Cnossen, I., Milan, S. E., Haaland, S., Coxon, J., Pedatella, N., et al. (2017). North–south asymmetries in Earth's magnetic field: Effects on high-latitude geospace. *Space Science Reviews*, *206*(1–4), 225–257. https://doi.org/10.1007/s11214-016-0273-0

McCaffrey, A., & Jayachandran, P. (2019). Determination of the refractive contribution to GPS phase "scintillation". *Journal of Geophysical Research: Space Physics*, *124*(2), 1454–1469. https://doi.org/10.1029/2018ja025759

Meziane, K., Kashcheyev, A., Patra, S., Jayachandran, P., & Hamza, A. (2020). Solar cycle variations of GPS amplitude scintillation for the polar region. *Space Weather*, *18*(8), e2019SW002434. https://doi.org/10.1029/2019sw002434

Moen, J., Oksavik, K., Abe, T., Lester, M., Saito, Y., Bekkeng, T., & Jacobsen, K. (2012). First in-situ measurements of hf radar echoing targets. *Geophysical Research Letters*, *39*(7), L07104. https://doi.org/10.1029/2012GL051407

Moen, J., Oksavik, K., Alfonsi, L., Daabakk, Y., Romano, V., & Spogli, L. (2013). Space weather challenges of the polar cap ionosphere. *Journal of Space Weather and Space Climate*, *3*, A02. https://doi.org/10.1051/swsc/2013025

Moen, J., Walker, I., Kersley, L., & Milan, S. (2002). On the generation of cusp HF backscatter irregularities. *Journal of Geophysical Research*, *107*(A4), SIA–3. https://doi.org/10.1029/2001JA000111

Noja, M., Stolle, C., Park, J., & Lühr, H. (2013). Long-term analysis of ionospheric polar patches based on CHAMP TEC data. *Radio Science*, *48*(3), 289–301. https://doi.org/10.1002/rds.20033

Oksavik, K., Moen, J., Lester, M., Bekkeng, T. A., & Bekkeng, J. K. (2012). In situ measurements of plasma irregularity growth in the cusp ionosphere. *Journal of Geophysical Research*, *117*(A11). A11301. https://doi.org/10.1029/2012ja017835

Pfaff, R. F., Jr., Marionni, P., & Swartz, W. E. (1997). Wavevector observations of the two-stream instability in the daytime equatorial electrojet. *Geophysical research letters*, *24*(13), 1671–1674. https://doi.org/10.1029/97GL01535

Prakash, S., Gupta, S., Subbaraya, B., & Jain, C. (1971). Electrostatic plasma instabilities in the equatorial electrojet. *Nature Physical Science*, *233*(38), 56–58. https://doi.org/10.1038/physci233056a0

Rino, C., Morton, Y., Breitsch, B., & Carrano, C. (2019). Stochastic TEC structure characterization. *Journal of Geophysical Research: Space Physics*, *124*(12), 10571–10579. https://doi.org/10.1029/2019ja026958

Ritter, P., Lühr, H., & Rauberg, J. (2013). Determining field-aligned currents with the Swarm constellation mission. *Earth, Planets and Space*, *65*(11), 1285–1294. https://doi.org/10.5047/eps.2013.09.006

Russell, C., & McPherron, R. (1973). Semiannual variation of geomagnetic activity. *Journal of Geophysical Research*, *78*(1), 92–108. https://doi.org/10.1029/JA078i001p00092

Spicher, A., Clausen, L. B. N., Miloch, W. J., Lofstad, V., Jin, Y., & Moen, J. I. (2017). Interhemispheric study of polar cap patch occurrence based on Swarm in situ data. *Journal of Geophysical Research: Space Physics*, *122*(3), 3837–3851. https://doi.org/10.1002/2016JA023750

Spicher, A., LaBelle, J., Bonnell, J. W., Roglans, R., Moser, C., Fuselier, S. A., et al. (2022). Interferometric study of ionospheric plasma irregularities in regions of phase scintillations and HF backscatter. *Geophysical Research Letters*, *49*(12), e2021GL097013. https://doi.org/10.1029/2021GL097013

Spicher, A., Miloch, W., & Moen, J. (2014). Direct evidence of double-slope power spectra in the high-latitude ionospheric plasma. *Geophysical Research Letters*, *41*(5), 1406–1412. https://doi.org/10.1002/2014GL059214

Spogli, L., Ghobadi, H., Cicone, A., Alfonsi, L., Cesaroni, C., Linty, N., et al. (2021). Adaptive phase detrending for GNSS scintillation detection: A case study over Antarctica. *IEEE Geoscience and Remote Sensing Letters*, *19*, 1–5. https://doi.org/10.1109/lgrs.2021.3067727

Tröbs, M., & Heinzel, G. (2006). Improved spectrum estimation from digitized time series on a logarithmic frequency axis. *Measurement*, *39*(2), 120–129. https://doi.org/10.1016/j.measurement.2005.10.010

Tsunoda, R. T. (1988). High-latitude F region irregularities: A review and synthesis. *Reviews of Geophysics*, *26*(4), 719–760. https://doi.org/10.1029/RG026i004p00719

van der Meeren, C., Oksavik, K., Lorentzen, D. A., Rietveld, M. T., & Clausen, L. B. (2015). Severe and localized GNSS scintillation at the poleward edge of the nightside auroral oval during intense substorm aurora. *Journal of Geophysical Research: Space Physics*, *120*(12), 10–607. https://doi.org/10.1002/2015JA021819

Villain, J., Hanuise, C., & Beghin, C. (1986). ARCAD3-SAFARI coordinated study of auroral and polar F-region ionospheric irregularities. *Annales geophysicae*, *4*, 61–68.

Wang, H., Lühr, H., & Ma, S. (2005). Solar zenith angle and merging electric field control of field-aligned currents: A statistical study of the southern hemisphere. *Journal of Geophysical Research*, *110*(A3), A03306. https://doi.org/10.1029/2004JA010530

Wang, Y., Jayachandran, P., Ma, Y.-Z., Zhang, Q.-H., Xing, Z.-Y., Ruohoniemi, J., et al. (2022). Dependencies of GPS scintillation indices on the ionospheric plasma drift and rate of change of TEC around the dawn sector of the polar ionosphere. *Journal of Geophysical Research: Space Physics*, *127*(11), e2022JA030870. https://doi.org/10.1029/2022ja030870

Wang, Y., Zhang, Q.-H., Jayachandran, P., Moen, J., Xing, Z.-Y., Chadwick, R., et al. (2018). Experimental evidence on the dependence of the standard GPS phase scintillation index on the ionospheric plasma drift around noon sector of the polar ionosphere. *Journal of Geophysical Research: Space Physics*, *123*(3), 2370–2378. https://doi.org/10.1002/2017ja024805

Welch, P. (1967). The use of fast Fourier transform for the estimation of power spectra: A method based on time averaging over short, modified periodograms. *IEEE Transactions on audio and electroacoustics*, *15*(2), 70–73. https://doi.org/10.1109/TAU.1967.1161901

Wygant, J., Keiling, A., Cattell, C., Johnson, l. M., Lysak, R., Temerin, M., et al. (2000). Polar spacecraft based comparisons of intense electric fields and Poynting flux near and within the plasma sheet-tail lobe boundary to UVI images: An energy source for the aurora. *Journal of Geophysical Research*, *105*(A8), 18675–18692. https://doi.org/10.1029/1999JA900500

Yeh, K. C., & Liu, C.-H. (1982). Radio wave scintillations in the ionosphere. *Proceedings of the IEEE*, *70*(4), 324–360. https://doi.org/10.1109/PROC.1982.12313

Zheng, Y., Xiong, C., Jin, Y., Liu, D., Oksavik, K., Xu, C., et al. (2022). The refractive and diffractive contributions to GPS signal scintillation at high latitudes during the geomagnetic storm on 7-8 September 2017.